Cold Regions Science and Technology 191 (2021) 103373

Contents lists available at ScienceDirect

Cold Regions Science and Technology

journal homepage: www.elsevier.com/locate/coldregions

Effects of surface roughness on splashing characteristics of large droplets with digital inline holographic imaging

Qiao Wang [a], Xiaodan Lin [c], Yujing Lin [a,*], Junlin Ma [b], Jingping Xiao [b], Yingchun Wu [c], Jian Wang [a]

[a] School of Engineering and the Environment, Kingston University London, London SW15 3DW, UK
[b] China Aerodynamics Research and Development Center, Mianyang 621000, China
[c] State Key Laboratory of Clean Energy Utilization, Zhejiang University, Hangzhou, 310027, China

ARTICLE INFO

Keywords:
Large droplets
Surface roughness
Splashing
Secondary droplets
Digital holography

ABSTRACT

Ice accretion on aircraft wings due to Supercooled Large Droplet (SLD) has a significant impact on flight safety. The dynamic behaviours of large droplet, such as deformation, breakup and splashing, have significant effects on icing accretion. The corresponding studies have been carried out experimentally and numerically, and empirical models to predict the dynamic behaviours of large droplets have been proposed. However, few empirical models involve surface roughness effects, especially its effects on the secondary droplets during icing accretion. In this paper, an experimental investigation on the impact of droplets onto surfaces with different roughness was conducted by using the high-speed Digital Inline Holography (DIH). The rapid splashing processes of droplets with Weber number around 570 and Mundo impact parameter K around 240 were captured and reconstructed based on a wavelet-based algorithm. Results show that DIH is suitable to diagnose the secondary droplets with a wide size range and record their velocities and locations. The roughness of the impact surface has a positive effect on the dynamics of splashing droplets, and the parameters including diameter, velocity, splash angle, splash height and mass-loss rate of splashing droplets rise with the increase of roughness. The new empirical correlations of the splashing characteristics of secondary droplets were fitted and developed, which could be used to update the current icing simulation models to take into account the effect of impact surface roughness on large droplets dynamics. This fundamental study may also be applied to the industrial applications including wind turbine icing, inkjets, sprays, as well as the erosion and formation of ice layers.

1. Introduction

Understanding the mechanisms of water droplet dynamics is of importance in the simulation of ice accretion. When impacting on a solid surface, large droplets possess significant dynamics characteristics, which are mainly manifested as deformation, breakup, spreading and splashing. These dynamics would affect droplet size, trajectory and water catch of an icing event. One of the applications is in aircraft icing. Aircraft could sometimes encounter special icing clouds containing the so-called Supercooled Large Droplets (SLDs) (maximum diameter >100 μm), which is described in the appendix O (EASA, 2015). In general, icing characteristics of SLD are significantly different from that of small droplets (Van Zante, 2007). The impingement limits are significantly aft than for the smaller droplets. The secondary droplets may re-impinge at the aerofoil trailing edge, or more seriously, impinge at the horizontal tail, increasing the water collection. This ice accretion problem also exists in wind turbine fields in cold regions when freezing rain drops impact on the blade of a wind turbine. Consequently, it may result in problems such as power losses, mechanical failures, and safety hazard. Dynamics of droplet have been studied and applied in many other industries such as structures icing, inkjets, sprays, combustion and soil erosion. Therefore, it is indispensable to investigate the dynamics characteristics of large droplets impacting on a solid surface, as well as their effects on the icing of structures in cold regions.

The study on droplet dynamics started more than 140 years ago (Worthington, 1877) but only becomes active and feasible due to the development of high-speed photograph. It enables time-resolved observation and analysis of droplet morphology, thus deepens the understanding on droplets dynamics. Past research has concluded that water droplet's impact and splashing process is mainly controlled by the following dimensionless groups, as summarized in ref. (Luxford, 2005):

* Corresponding author.
E-mail address: y.lin@kingston.ac.uk (Y. Lin).

https://doi.org/10.1016/j.coldregions.2021.103373
Received 4 February 2021; Received in revised form 26 May 2021; Accepted 27 July 2021
Available online 30 July 2021

List of symbols

d_0	Diameter of incident water droplet, μm
d_n	Diameter of springe needle, μm
d_s	Diameter of secondary droplet, μm
$\overline{d}_s$	Average diameter of secondary droplets, μm
f	Mass loss rate during splashing
h	Splashing height, μm
$\overline{q}$	The arithmetic mean of individual observations
K	Mundo impact parameter
K_c	Critical impact parameter
Ra	Surface roughness amplitude, μm
St	Dimensionless surface roughness
V_0	Incident velocity of water droplet, m/s
$\overline{V_s}$	Average velocity of secondary droplets, m/s
$V_{s,\,n}$	Average normal velocity of secondary droplets, m/s
$V_{s,\,t}$	Average tangential velocity of secondary droplets, m/s
V_∞	Air flow velocity, m/s
Oh	Ohnesorge number
Re	Reynolds number
We	Weber number
α	The maximum spreading factor
β	Average dimensionless diameter of secondary droplets
γ	Average dimensionless splashing velocity of secondary droplets
γ_n	Normal component of γ
γ_t	Tangential component of γ
η	Average dimensionless height of secondary droplets
θ_0	Incident angle of water droplet, $^\circ$
θ_s	Splashing angle of secondary droplet, $^\circ$
λ	Wavelength of the instability, m
μ_d	Viscosity of water droplet, kg/ms
ρ_d	Density of incident water droplet, kg/m^3
σ_d	Coefficient of surface tension of water, kg/s^2
τ	Dimensionless time
ϕ	Average dimensionless splashing angle of secondary droplets

Reynolds number:

$$Re = \frac{\rho d_0 V_0}{\mu} \tag{1}$$

Weber number:

$$We = \frac{\rho d_0 V_0^2}{\sigma} \tag{2}$$

Ohnesorge number:

$$Oh = \frac{\mu}{(\rho\sigma d_0)^{1/2}} = \frac{We^{1/2}}{Re} \tag{3}$$

Mundo impact parameter:

$$K = Oh \bullet \mathrm{Re}^{1.25} \tag{4}$$

where ρ, μ and σ are the density, viscosity, and surface tension of the water droplet. d_0 and V_0 are the diameter and impact velocity of the water droplet, respectively.

For the experimental studies of droplet impingement dynamics, the maximum spreading factor α (the diameter ratio between the largest spreading circle and the initial water droplet), the splashing threshold and the characteristics of secondary droplets (diameter, velocity, mass ratio, and etc.) are the main characteristics of droplet impact and splashing to be studied. One of the earliest studies was performed by Stow and Hadfield (1981), who presented an investigation on water droplet impact upon a dry surface. They found that the maximum spreading is independent of roughness, and the critical value K_c of droplets splash depends on the surface roughness. Mundo et al. (1995) proposed critical impact parameter $K_c > 57.7$ as splashing threshold and found that for rough surfaces the splashing occurs under the influence of the local surface angle, leading to a transfer of tangential momentum into normal momentum. Cossali et al. (1997) developed an empirical correlation between impact parameter K_c and roughness Ra based on the data from Mundo et al. (1995) and Yarin and Weiss (1995). Range and Feuillebois (1998). Roisman et al. (2015) found the splashing threshold is related to a critical Weber number which depends on the characteristic slope of the roughness. Mehdizadeh et al. (2004) found that both the number of fingers and the maximum extent of spreading were decreased with the increase of surface roughness. Xu et al. (2007) and Latka et al. (2012) studied the interplay of surface roughness and air pressure on the mechanisms of splashing and found that splashing can be completely suppressed by decreasing the pressure of the surrounding gas. Recently, Castrejón-Pita et al. (2016) and Quetzeri-Santiago et al. (2019a, 2019b) carried out many experiments to investigate the behaviour of a droplet impacting on moving liquids and the effect of surface roughness on dynamic contact angle and splashing. Li et al. (2019) investigated the effect of Weber number and the dimensionless film thickness on the features of the secondary droplets by a high-speed camera. Various splashing thresholds were reviewed by Moreira et al. (2010) and Josserand and Thoroddsen (2016), and they concluded that the discrepancies between the proposed splashing thresholds were due to the fuzzy definition of the splashing boundary and the surface roughness.

For the numerical studies of droplet impingement dynamics, finite volume method and volume-of-fluid approach are the main numerical methods. One of the typical codes is the open-source package Gerris (Popinet, 2003, 2009), which can accurately solve the incompressible Navier–Stokes equations and account for fluid-fluid and fluid-solid interfaces. Cimpeanu and Papageorgiou (2018) conducted a numerical study on droplet impact by direct numerical simulations (DNS) using the volume-of-fluid method in three dimensions. New morphological features were identified. Pegg et al. (2018) presented a mathematical study on droplet impacting onto an elastic plate and demonstrated the effect of substrate oscillation on splashing. As Cimpeanu and Papageorgiou (2018) mentioned, however, many of the assumptions in droplet dynamics simulation become inaccurate in the context of the large supercooled droplets (larger than several tens of microns) found in the atmosphere. Thus, for aircraft icing application, a series of experiments to derive semi- empirical relations of large droplet impact and splashing have been carried out (Papadakis et al., 2007a, 2007b, 2013; Papadakis and Wong, 2006; W. Wright and Potapczuk, 2004).

For the characteristics of secondary droplets, the development of relations or models for droplet impact onto dry surfaces mainly depends on the measurement technologies, which has been reviewed by Yarin (2006), Thoroddsen et al. (2008) and Moreira et al. (2010). Phase-Doppler Anemometer (PDA) (Mundo et al., 1995; Weiss, 2005) is mainly for droplet impact and splashing process. High-speed camera (Cossali et al., 1997; Pan et al., 2010; Range and Feuillebois, 1998) is mainly for both fuel sprays and single droplet impact fields. The information of secondary droplets sizes and velocities are obtained from post-process based on different algorithms. However, very limited data on secondary droplet sizes and velocities are available in open literatures. This may be due to that PDA and high-speed camera are both based on a two-dimensional (2D) method, making many secondary droplets out of focus and difficult to calculate their exact positions and velocities.

Additionally, the mass loss are usually measured by setting a white paper to collect secondary droplets, but some secondary droplets could fall at the same point which could make big errors (Stow and Hadfield, 1981; Xu et al., 2007). Based on the measurement technologies reviewed above, the models of secondary droplets were derived by Mundo et al. (1995) and Trujillo et al. (2000) and are presented in Table 1, respectively.

In recent years, 3D imaging, such as digital inline holography (DIH), has been employed to investigate droplet dynamics. Both amplitude and phase of the scattered object waves can be recorded in hologram. Through holographic reconstruction, the diameter, position, velocity and other related variables of splashing droplets can be measured accurately. Guildenbecher et al. (2014) applied DIH technology and adopted a new-developed hybrid method of particle detection to quantify secondary droplets upon impact of a single droplet on a thin film. Wu et al. (2014) proposed a wavelet-based algorithm to extend the depth-of-field and to locate the 3D position in digital inline particle holography, which makes it possible to obtain the 3D vector field and 3D position of the particle accurately in the high-frequency sub-images. Additionally, DIH has been used widely in the studies of fuel sprays and particles in combustion (Wu et al., 2017; Yao et al., 2015, 2018), which has confirmed that DIH method is suitable to detect the secondary droplets within a wide range of size accurately. Despite the significant advantages, few studies have been done on droplet splashing dynamics upon the rough surface with DIH.

In short, due to the limitations of technical methods, few experimental data on secondary droplet characteristics upon rough surface are obtained from high-speed three-dimensional fields. Therefore, it is imperative to obtain those data and develop a more accurate splashing model accounting for the surface roughness effect on splashing droplet dynamics.

In present study, influences of impact surface roughness on the dynamics of splashing droplets in three-dimension is investigated by conducting high-fidelity experiments with DIH. In Section 2, the methodology used in the present experimental study is detailed. The experimental data is presented and analysed qualitatively. Corresponding correlations are thus developed from experiments to present the effect of surface roughness on various splashing characteristics, as presented and discussed in Section 3. These correlations could be used in developing droplet impingement models under roughness effects.

2. Methodology

2.1. Experimental set-up

Fig. 1 shows the layout of the experimental apparatus, which consists of two main parts - water droplet generation system and digital holographic measurement system.

Droplets are produced at the tip of a needle and driven by a syringe pump. The size of droplets and the time interval releasing a droplet are controlled by the diameter of the syringe needle's end and water volumetric flow rate. Due to the surface tension effect, the syringe needle would collect a large amount of water before the droplet drips under the effect of gravity. The diameter of the droplet can be defined according to the balance of its gravity and surface tension, $\pi {d_0}^3 \rho_d g/6 = \pi d_n \sigma_d$, where ρ_d and d_0 are the water droplet density and diameter, respectively. d_n is the diameter of the needle and σ_d is the surface tension coefficient. According to the existing studies (Josserand and Thoroddsen, 2016; Wierzba, 1990; Yarin, 2006), the droplet generator was designed to produce droplets with a diameter at millimetres level, between 2600 μm and 2700 μm for the present work. This diameter range is at the same level as the upper limit of freezing rain's diameter defined in the SLD icing envelop. The time interval of releasing each droplet Δt can be given by $q\Delta t = \pi {d_0}^3/6$ based on mass conservation, where q is the water volumetric flow rate and was set to 3 ml/h for the current study. Δt is primarily used to trigger each recording to guarantee all the measurements can be in a temporal phase and can be directly compared.

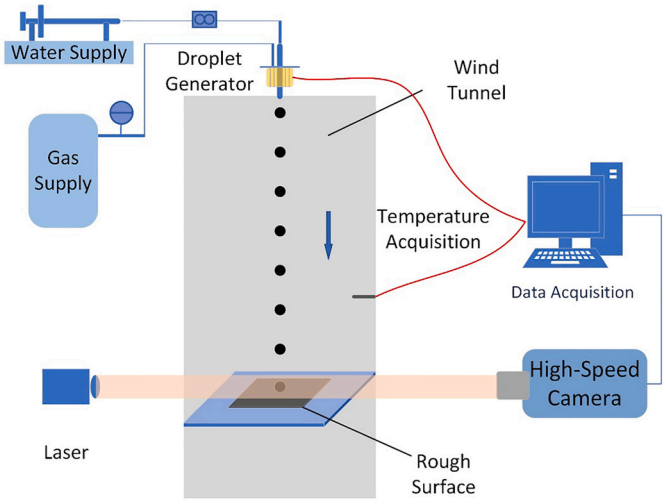

Fig. 1. Schematic of the experimental system.

Fig. 1 also illustrates the schematic of the measurement system of DIH. A laser beam with a wavelength of λ = 532 nm is emitted by the continuous laser generator (OXXIUS LCX-532S-300). The laser beam is then filtered with spatial filtering and collimated with a spherical lens into a plane wave, with the beam diameter expanded to approximately 50 mm. A high-speed camera (LaVision High-Speed Star 500 K-M3) is operated at 3500 frames per second (FPS) to record the time-resolved hologram of the impact event. The exposure time is set as 3 μs to suppress the motion blur, and the hologram has a resolution of 1024 × 1024 pixels and a pixel size of 20 μm. Thus, the size of field-of-view is approximately 20 mm × 20 mm × 65 mm. In addition, two temperature sensors are set at the test section and the nozzle port, in order to measure the temperatures of the airflow and water droplet in real time, respectively. A PC is connected for data acquisition and analysis simultaneously.

Table 1
Test conditions and related parameters

	Mundo et al. (1995)	Trujillo et al. (2000)
Splashing threshold	$K_c = Oh^{-0.4}We$	$K_{L,\,n} > 17$
Number of secondary droplets	$n_s = 1.676 * 10^{-5}K^{2.539}$, $n_s \le 1000$	/
Size of secondary droplets	$\frac{d_s}{d_0} = 8.72e^{-0.0281K}$, $0.05 \le \frac{d_s}{d_0} \le 1$	$\frac{d_s}{d_0} = 8.72e^{-0.0281K}$, $0.05 \le \frac{d_s}{d_0} \le 1$
Mass loss	$\frac{m_s}{m_0} = n_s\left(\frac{d_s}{d_0}\right)^3$	$\frac{m_s}{m_0} = 0.2\left[1 - exp\left(0.85^*\left(K_{L,n} - 17\right)\right)\right]$
Velocities of secondary droplets	$\frac{V_{s,t}}{V_{0,t}} = 1.337 - 1.318\frac{d_s}{d_0} + 2.339\left(\frac{d_s}{d_0}\right)^2$	$\frac{V_{s,t}}{V_{0,t}} = 1.075 - 0.0025\theta_0$
	$\frac{V_{s,n}}{V_{0,n}} = -0.249 - 2.959\frac{d_s}{d_0} + 7.794\left(\frac{d_s}{d_0}\right)^2$	$\frac{V_{s,n}}{V_{0,n}} = 0.3 - 0.002\theta_0$

2.2. Hologram recording and reconstruction

Digital inline holography (DIH) approach consists of two steps: digital recording and numerical reconstruction, as shown in Fig. 2. When a particle is illuminated by a collimated laser beam, the scattered light, as the object wave, interferes with the undisturbed reference wave and the interference pattern is recorded by the camera to form a digital particle hologram. The hologram is reconstructed slice by slice along the depth direction with a wavelet reconstruction method, which is based on scalar diffraction theory, to revive the 3D optical particle field. A slice image can be reconstructed by the convolution of the hologram and the wavelet function is as follows:

$$\boldsymbol{I}(x,y,z) = 1 - \boldsymbol{I}_{holo}(x,y) \otimes \Psi_z(x,y) \tag{5}$$

where I(x, y, z) is the intensity of the reconstructed 3D particle field, $\otimes$ is the convolution. $\boldsymbol{I}_{holo}(x,y)$ and $\Psi_z(x,y)$ denotes the particle hologram and the wavelet function, respectively. To eliminate the influence of large particles on small particles, a two-step detection method is adopted. Large drops are first characterized and simulated by a diffraction-based model (Yao et al., 2015). The method of locating the axial positions of both opaque and transparent objects to extend the wavelet-based depth-of-field are applied here, as proposed by Wu et al. (2014). The methods were validated by simulated holograms and experimental results. The absolute diameter error is no more than 20 μm, and the average value of z position error is approximately 0.18 mm. It is confirmed that DIH was suitable to diagnose the secondary droplets with a wide size range from an acoustically levitated drop (Yao et al., 2015).

The reconstructed 3D optical particle field is processed to retrieve the particle 3D position, diameter and 2D shape and velocity. Firstly, a depth-of-field extended image is synthesized by using a wavelet fusion algorithm (Wu et al., 2014), in which all the particles in the reconstructed 3D optical field are focalized. The synthesis image is then binarized by applying a proper threshold to separate the particles from the background. The transverse location and pixels occupied by particles can be obtained by edge extraction with subpixel accuracy. To minimize the effects of particle noise and abnormal deformation, only the particles with solid degree more than 0.8 and length-width ratio between 1 and 3 are accepted. Through this treatment, the actual size of particles can be obtained according to the actual size represented by the calibrated pixels. Next, the particle's depth position is evaluated from its focus metric curve, which is the variance of the intensity gradient within its local window. In order to measure the particle velocity, digital holographic particle tracking velocimetry is employed. As described above, the particle field is exposed several times when the droplet is moving in the field of view of the digital inline holography. Series holograms are reconstructed, yielding the spatial position of droplets at different times. The droplets at the consecutive holograms are paired, and the droplet velocities are determined by dividing the 3D displacements at the corresponding time interval.

2.3. Experimental conditions

All the test cases in present study are listed in Table 2. Case 1 presents droplets impact upon a smooth substrate, and case 2 to 6 are for the rough substrate with reducing roughness. From case 2a to case 2e, all the conditions including roughness keep the same for repeated tests. The experimental roughness *Ra* is represented using standard sandpapers, ranging from 2.6 μm to 250 μm as shown in Fig. 3. Roughness *Ra* refers to the arithmetic mean of the absolute values of vertical deviation from the mean line through the surface profile and is characterized in unit of μm (Bhushan, 2000). The diameters and velocities of the water droplets are determined from measurement data. Note that based on Luxford's study (Luxford, 2005), water temperature affects its surface tension but much less than viscosity. Value of surface tension at −20 °C is approximately 8% higher than that at +20 °C, so the water temperature may not have a significant effect on the strong impact process in the current problem. Therefore, the experiments are conducted under ambient temperature, which is approximately 15 °C. It is noted that, for each test condition, five repeated impact events are carried out and analysed in order to guarantee the convergence of the statistical values. The substrate surface is treated to be always dry before each test to guarantee there is no residual water.

2.4. Measurement of secondary droplets characteristics

This section presents how the main secondary droplets characteristics, such as diameter, velocity and total mass, are derived from DIH results. The reconstructed 3D optical particle field is processed to retrieve the particles' 3D positions and diameters. Firstly, a depth-of-field extended image is synthesized by adopting a wavelet fusion algorithm (Yao et al., 2015), in which all the particles in the reconstructed 3D optical field are focalized. The synthesis image is binarized by applying a proper threshold to separate the particles from the background. The transverse location and pixels occupied by particles can be obtained by edge extraction with subpixel accuracy. Through this process, the actual size of particles can be obtained according to the actual size represented by the calibrated pixels. The measurement error for the secondary droplet's diameter d_s was estimated less than 20 μm (Yao et al., 2015).

In order to obtain the particle velocity, the particle field inside the field-of-view of DIH are exposed several times, and the series of holograms are reconstructed, yielding the spatial position of droplets at different times. Then, the droplets at the consecutive holograms are paired, and their velocity vectors are then determined by $\boldsymbol{V} = \Delta\boldsymbol{x}/\Delta t$ where $\Delta\boldsymbol{x}$ is the drops' 3D displacement. Consequently, velocity error depends on position error. Since the transverse position (x-y position) is easy to determine with high precision (Guildenbecher et al., 2014; Yao et al., 2015), the error of droplet's position mainly comes from the depth direction (z-direction). The average measurement error of particle's depth position was estimated approximately 0.18 mm by Yao et al.

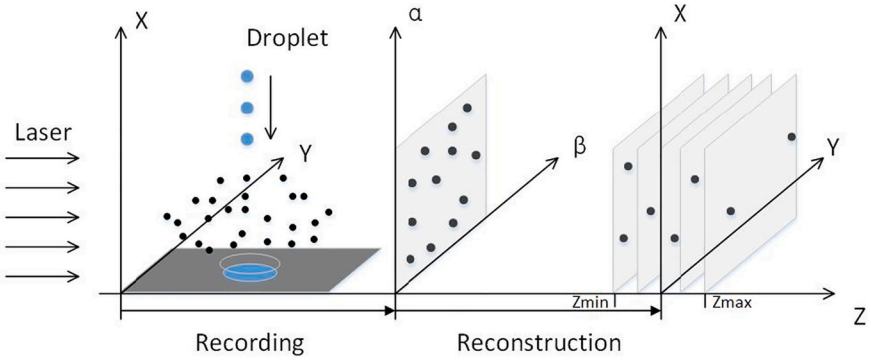

Fig. 2. Schematic of Digital In-line Holographic Recording and Reconstruction.

Table 2
Test conditions and dimensionless parameters.

Cases		d_0 (μm)	V_0 (m/s)	Sandpaper grit	Ra (μm)	St	We*	Re*	K
1		2690 ± 20	3.82 ± 0.1	None	smooth	None	534	9013	225 ± 5
2	2a	2660 ± 20	4.06 ± 0.1	60	250	0.0940	596	9472	241 ± 3
	2b	2630 ± 20	4.06 ± 0.1	60	250	0.0951	589	9365	239 ± 3
	2c	2690 ± 20	4.03 ± 0.1	60	250	0.0929	594	9508	241 ± 3
	2d	2670 ± 20	4.06 ± 0.1	60	250	0.0936	598	9508	242 ± 3
	2e	2680 ± 20	4.05 ± 0.1	60	250	0.0933	597	9520	241 ± 3
3		2650 ± 20	4.02 ± 0.1	80	178	0.0672	582	9344	237 ± 4
4		2660 ± 20	4.05 ± 0.1	120	124	0.0466	593	9449	240 ± 3
5		2670 ± 20	3.96 ± 0.1	500	25	0.0094	569	9274	234 ± 4
6		2670 ± 20	4.05 ± 0.1	5000	2.6	0.0010	595	9484	241 ± 3

* At 15 °C, ρ and σ of water are 999 kg/m^3 and 0.0735 N/m, respectively (Crittenden et al., 2012).

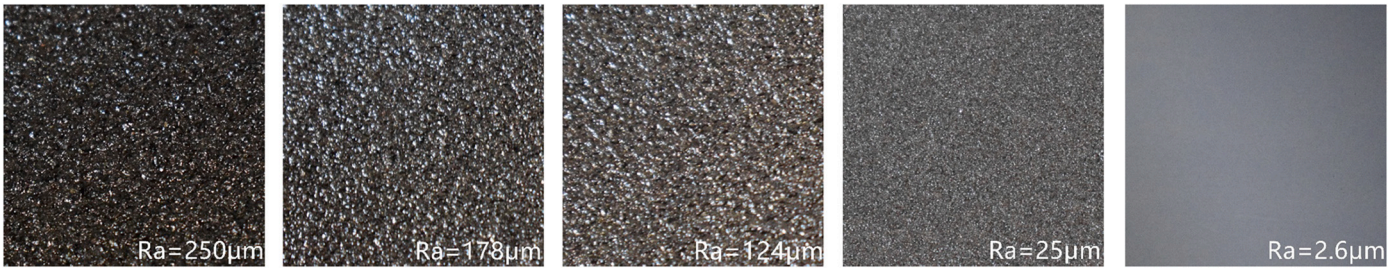

Fig. 3. Average diameter changes of secondary droplets during splashing.

(2015), and it thus can be converted to the velocity error of the secondary droplet in z-direction by dividing $\Delta t = 1/3500$s, which is approximately 0.63 m/s.

The ratio of total mass of secondary drops to the mass of primary drop is defined as the mass loss rate and given by

$$f = \frac{1}{d_0^3}\sum_{n=1}^{N} d_s^3 \tag{6}$$

where d_s and N denotes the diameter and number of all the visible secondary droplets, respectively. Undoubtedly, it is very difficult to include all the splashing droplets, so the earliest stable time will be selected to count the splashing drops number, which allows as many droplets as possible to be captured. Also, at the early stage of splashing, only very small drops, approximate 5% with diameters below 50 μm, have a relative high speed to get out of the field-of-view which would have a minimal impact on mass loss rate.

3. Results and discussion

3.1. Analysis of experimental repeatability and uncertainty

Five repeated tests, from case 2a to 2e in Table 2, were conducted to verify the repeatability of the experiment, and all repeated cases have the same surface roughness of $Ra = 250$μm. Then, the reliability of the repeated results was verified through the following two aspects: comparison of the secondary droplet size distributions and evaluation of splashing parameters' relative standard deviation (RSD), also known as

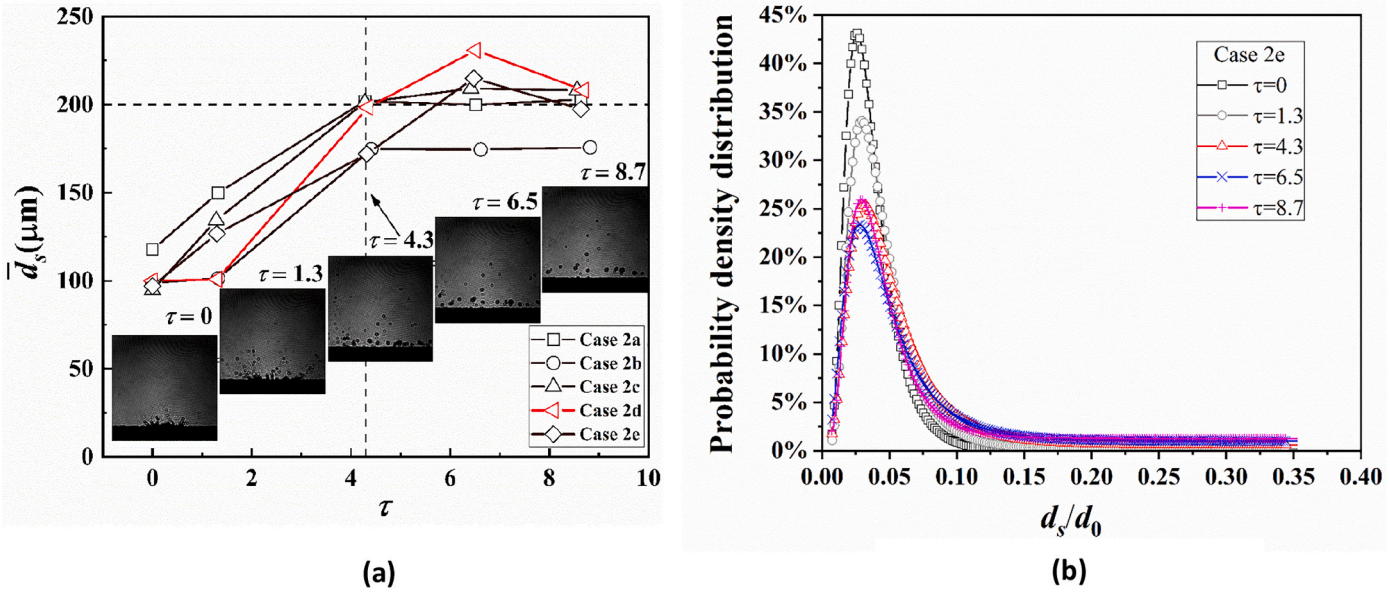

Fig. 4. Average diameter changes and probability density of secondary droplets during splashing.

the coefficient of variation (Skrondal and Everitt, 2010).

Fig. 4(a), with five serial holographic images of case 2d presented, shows the average diameter $\overline{d}_s$ of the secondary droplets at five different time $\tau = 0.0, 1.3, 4, 3, 6.5, 8.7$ for case 2a to 2e. The dimensionless time τ is defined as $\tau = tV_0/d_0$, where t is the impact time and $t = 0 \pm 0.286$ms refers to the first frame that splashing occurs. It can be seen that all five cases show almost the same trend in terms of the relationship between $\overline{d}_s$ and τ. The average diameter $\overline{d}_s$ initially rises with time and becomes stable as well as the probability density of d_s after approximately $\tau = 4.3$, as shown in Fig.4(b). Thus, the earliest stable time $\tau = 4.3$ was selected to analysis distributions of the secondary droplet size. Fig. 5 shows the probability density distribution and its lognormal fit of the secondary droplet sizes d_s/d_0 for case 2e at $\tau = 4.3$. By using the same approach, five lognormal fit curves of the relative frequency corresponding to the five repeated test cases are plotted together and compared in Fig. 6. It shows a good agreement between five cases with a maximum of 25% possibility for the secondary droplets' sizes ranging between 0.024 and 0.025. From Fig. 5 and Fig. 6 we can also see that, the measured probability density tends toward zero at the limit of large and small diameters. This means that almost all of the secondary drops size are captured and the results are statistically converged.

Another measure of the repeatability is the RSD of the splashing parameters including diameter, velocity and angle of the secondary droplet. RSD is calculated based on Type A standard uncertainty (JCGM and others, 2008) and given by:

$$RSD = \frac{s(q_k)}{\overline{q}} * 100\% \tag{7}$$

where $\overline{q}$ is the arithmetic mean of the individual observations, q_k is the splashing parameter, $s(q_k)$ is the experimental standard deviation according to:

$$s^2(q_k) = \frac{1}{n-1}\sum_{j=1}^{n}(q_j - \overline{q})^2 \tag{8}$$

Figs. 7 and 8 show all the statistical results of the secondary droplets' diameters, velocities, and splashing angles for the five repeated tests during the timescale $\tau = 1.3 \sim 8.6$. The dimensionless diameter β, ϕ and St are defined as $\beta = \overline{d}_s/d_0$, $\gamma = \overline{V}_s/V_0$, $\phi = \overline{\theta}_s/\theta_0$ and $St = Ra/d_0$ respectively, where $\overline{d}_s$, $\overline{V}_s$ and $\overline{\theta}_s$ are the average diameter, velocity and

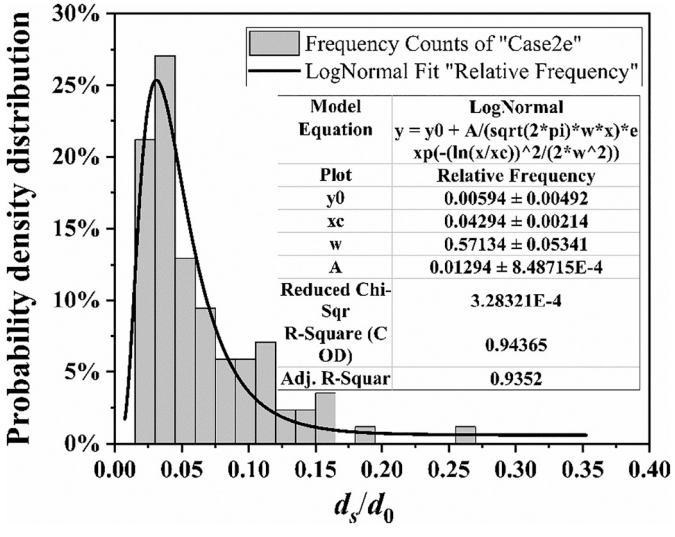

Fig. 5. Probability density distribution of the secondary droplets sizes for Case 2e (τ = 4.3).

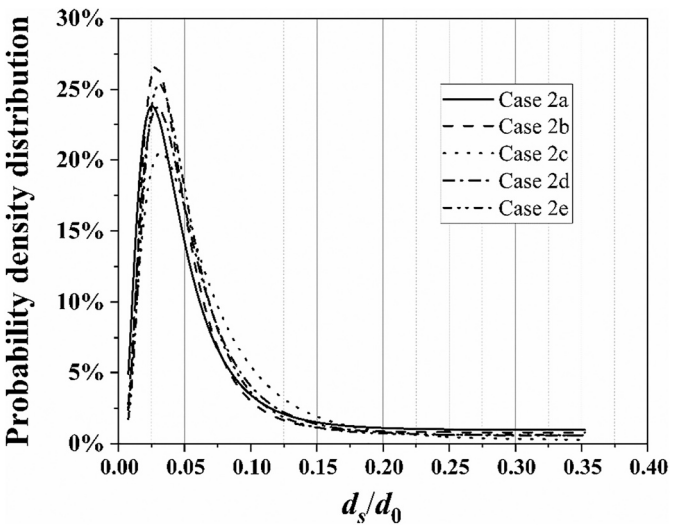

Fig. 6. Distributions of the secondary droplets sizes for five repeated cases (τ =4.3).

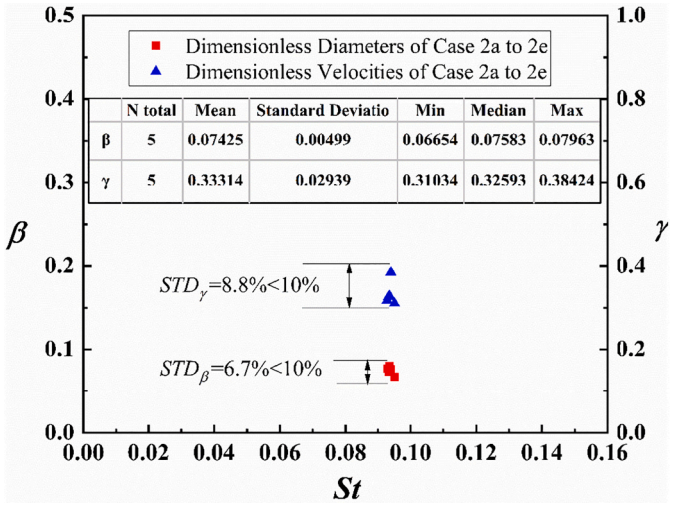

Fig. 7. Statistical results of the average secondary droplets' diameter and velocity.

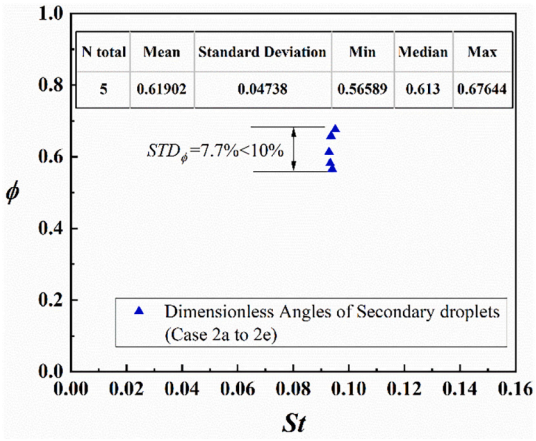

Fig. 8. Statistical results of the average secondary droplets' splashing angle.

splashing angle of the secondary droplets, respectively. Since the water droplet falls and impacts upon the test substrate vertically, the incident angle $\theta_0 = 90^\circ$. It is seen that the RSDs for dimensionless diameter, velocity and splashing angle are all less than 10%. Also, the statistical results shows that, the standard deviation of the uncertainty of average secondary droplets' diameter β, velocity γ and splashing angle ϕ are 0.005, 0.029 and 0.047, respectively. Thus, the results of repeated experiments are generally consistent and repeatable for the present study, which indicates that the experimental system is stable and the experimental data are reliable.

3.2. Effect of surface roughness on 3D splashing characteristics

Figs. 9 and 10 give the hologram (top row) and their reconstructed images (bottom row) of case 1 and case 2d, respectively. Both cases have the same test conditions, but different surface roughness ($St \approx 0$ for case 1 and $St = 0.0936$ for case 2d). The dimensionless time τ used for recording is labelled on the upper-right corner of the image, and as defined above. The colours of secondary droplets in the reconstructed images in Fig. 10 represent their distances from the focal plane in the depth direction of z, which range from 230 mm (cold colour) to 300 mm (warm colour).

From Fig. 9, it can be seen that on the smooth aluminium substrate (case 1, $St \approx 0$), droplet only spreads with slight fluctuations after impacting and there are no splashing droplets, which is also known as deposition. A thin water film is eventually formed on the substrate later. Fig. 10 (case 2d, $St = 0.0936$), however, shows a typical prompt splashing process upon a rough and dry substrate and a large number of secondary droplets are produced and splash in different directions, which indicates the significant effect of surface roughness on droplet's splashing behaviours. Furthermore, Fig. 11 shows a zoom-in picture recorded at time $\tau = 8.6$ in case 2e ($St = 0.0933$) and its 3D representation, which clearly illustrates the whole picture and distribution of the measured secondary droplets.

Based on the hologram and holographic reconstruction maps for each case, the splashing diameters, velocities, angles and heights of secondary droplets could be derived and their variations with surface roughness are then analysed and presented in the following sub-sections. Following the same modelling method in ref. (Tang et al., 2017; Yarin, 2006), empirical models regarding roughness effect on droplets splashing characteristics will be proposed in the form:

$$y \sim St^a \bullet (\ln \mathrm{St})^b \ (0.001 < \mathrm{St} < 0.1) \tag{9}$$

where a and b are constants, and y corresponds splashing droplets characteristics.

3.2.1. Splashing diameters of secondary droplets

Fig. 12 shows the dimensionless diameter β of secondary droplets at different roughness St conditions, corresponding to case 2 to 6. Here, the value of case 2 is the mean value of case 2a to 2e, and the symbols show the mean of each roughness condition, while the error bars show the minimum and maximum, and this is also applied to the following sections. Note that for Case 1, $St = 0$ seems like a singularity point and thus not following the curve trend. The variation of secondary droplet size with roughness is validated by comparing with the results in Stow and Hadfield (1981). It is found that β increases with roughness St in the range of $St = [0.001, 0.1]$, which is consistent with the conclusion of Stow and Hadfield (1981). It is also found that the splashing threshold model is improved compared to that in Stow and Hadfield (1981), as shown in Fig.13 (Wu, 1992).

We then compare our results with Mundo model (Moreira et al., 2010; Mundo et al., 1995; Wright, 2005), in which the effect of surface roughness is not considered, as shown in Fig. 14. The blue and red solid line present Mundo model and our experimental results, respectively.

$$\beta = \begin{cases} 8.72e^{-0.0281K} & 77 < K < 183.68 \\ 0.05 & K > 183.68 \end{cases} \tag{10}$$

Eq. (10) gives the prediction model of LEWICE, where the diameter β does not change with K anymore when $K > 183.68$ and keeps at a constant 0.05. However, as surface roughness being taken into account in the present study, the results show that β does not keep as a constant for different impact parameter K. Instead, it changes with a combined effect of impact parameter K and surface roughness St. The larger roughness and higher impact parameter generally cause bigger secondary droplets. With the same impact parameter, the secondary droplet diameter increases significantly with surface roughness.

Here, our understanding on the physical mechanisms behind these phenomena is given. It is evident that secondary droplets are mainly produced by the jets on the rim of the crown and their number and size are determined by the initial perturbations (Yarin and Weiss, 1995). For the smoother surface with $St<0.01$, the incident droplet can rapidly spread and form a thinner lamella due to less frictional force. According to Levin (1970) and Stow and Stainer (1977), the criteria for jet producing a secondary droplet is $\lambda > \pi d_s$, where λ is the wavelength of the instability. Thus, smaller secondary droplets are produced from the thinner lamella. With the less frictional force on smoother surface, the rim can reach higher velocity due to less energy dissipation. Thus smaller secondary droplets with higher inertial force could overcome the surface tension and consequently formed. For the rougher surfaces with $St > 0.01$, as roughness promotes contact line instability, the size of the perturbations appearing on the rim increases under the combined effects of frictional force, surface tension and surrounding air. This could contribute to bigger secondary droplets and our conclusion is consistent

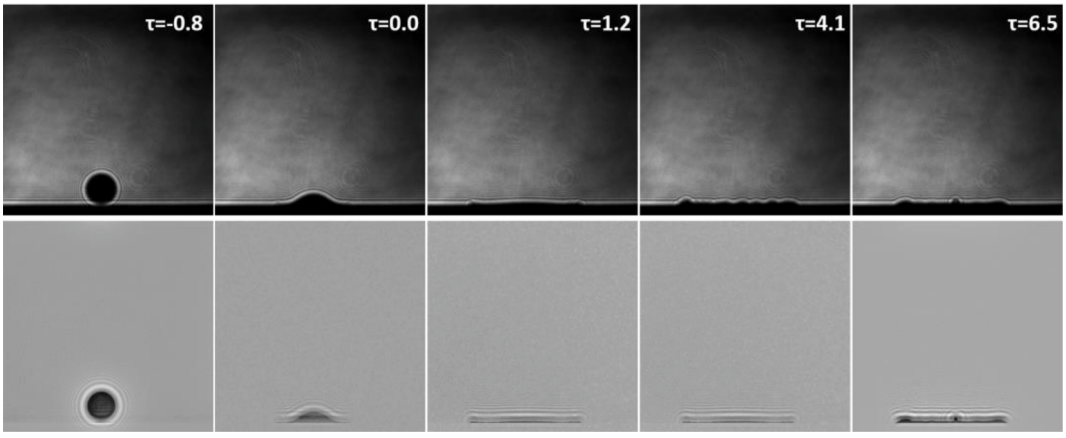

Fig. 9. The hologram (top row) and reconstructed binary grayscale images (bottom row) of Case 1 ($St \approx 0$).

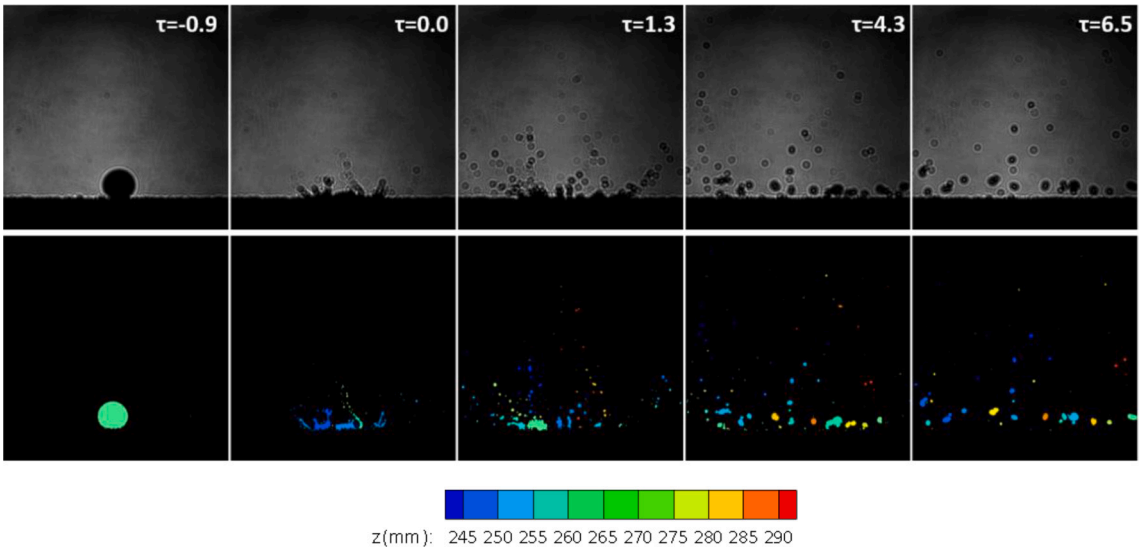

Fig. 10. The hologram (top row) and reconstructed contour images (bottom row) of Case 2d (t = 0.0936).

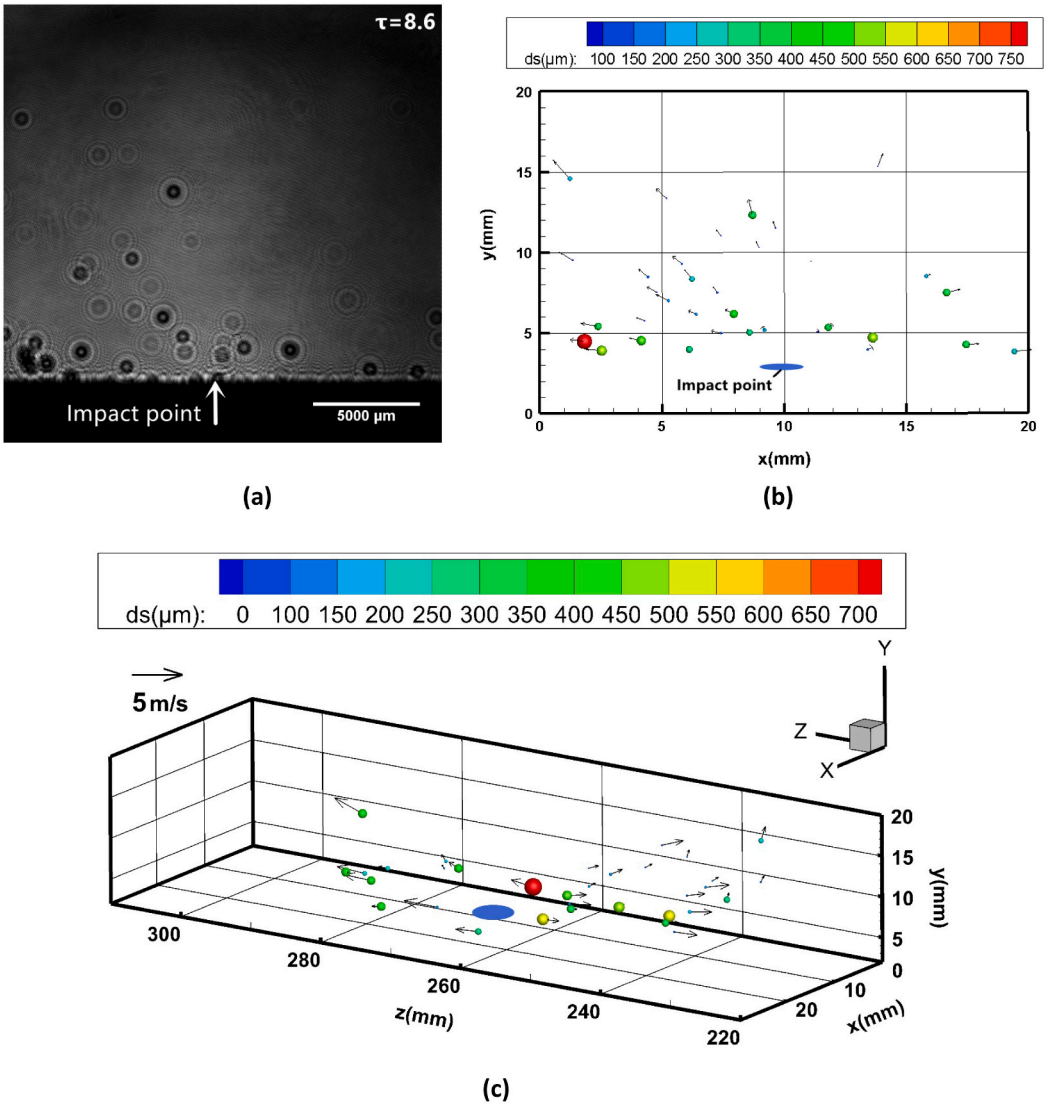

Fig. 11. (a) A zoom-in picture of Case 2e at τ = **8.6** (b) 2D representation of the splashing droplets plotted in x-y plane (c) 3D representation of the splashing droplets.

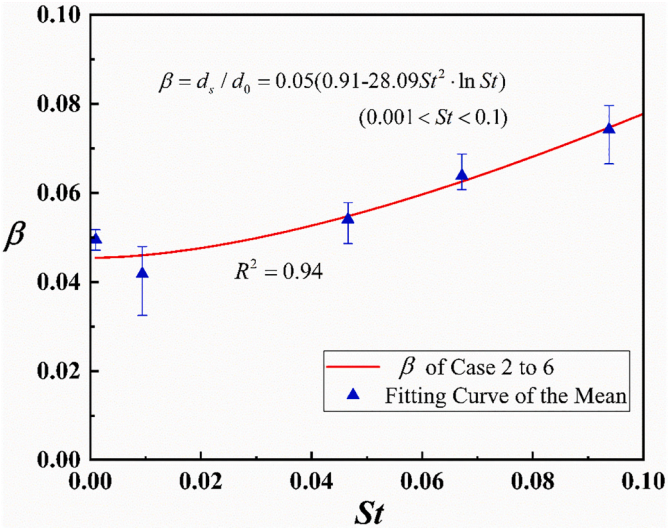

Fig. 12. Secondary droplets diameter β at different roughness *St*.

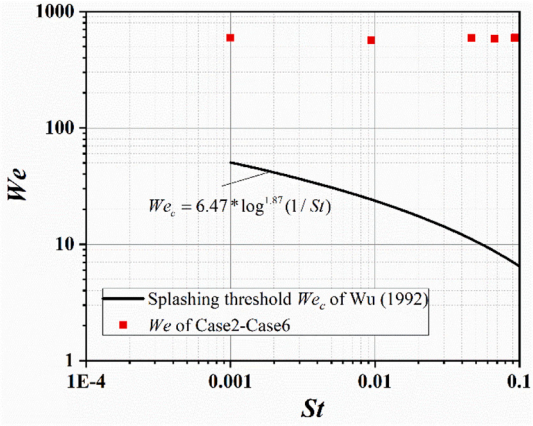

Fig. 13. Parameter space of *We* number vs *St* number

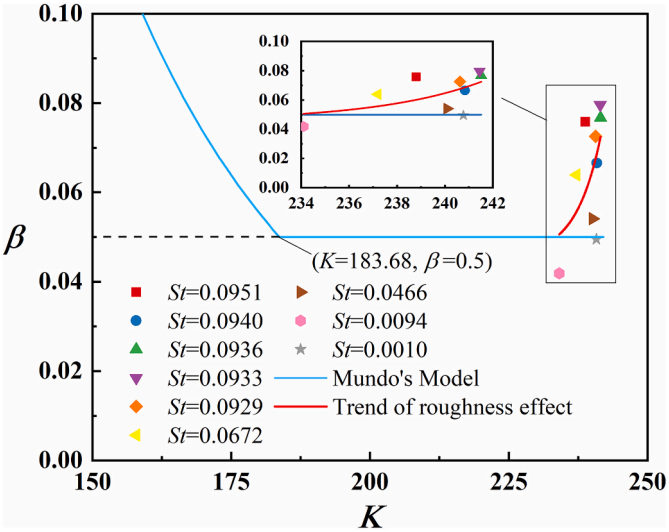

Fig. 14. Secondary droplet diameter β at different roughness *St* and impact parameter K

with the results of Range and Feuillebois (1998) and Stow and Stainer (1977). Other researchers have discussed the roughness effect on splashing through wettability and dynamic contact angle (De Goede et al., 2020; Quetzeri-Santiago et al., 2019a). However, the wettability, as mentioned by Wenzel or Cassie-Baxter (Belaud et al., 2015), cannot be determined within the present experiments, analysis on the wettability effect on diameters of secondary droplets will not be given here.

In short, surface roughness should be taken into account in droplet splashing process to improve the accuracy and reliability of dynamics simulation. A modified empirical correlation is given for $K > 183.68$, as below:

$$\beta = 0.05\left(0.91 - 28.09St^2 lnSt\right)\ 0.001 < St < 0.1 \tag{11}$$

3.2.2. Splashing velocities and angles of secondary droplets

For the present experiments, only velocities in the transversal (x-y) directions were determined and compared to the existing model LEWICE 3.2 (Wright, 2008). The dimensionless velocity components of secondary droplets in the x and y directions are defined as tangential and normal components, respectively:

$$\begin{cases} \gamma_n = V_{s,n}/V_{0,n} \\ \gamma_t = V_{s,t}/V_{0,t} \end{cases} \tag{12}$$

where $V_{s,\ n}$ and $V_{s,\ t}$ are the average normal and tangential velocity components of the secondary droplet. Since the incident droplet impacts upon the surface perpendicularly, the tangential component of primary droplet velocity $V_{0,\ t} = 0$ and $V_{0,\ n} = V_0$. In order to prevent division by zero, $V_{s,\ n}$ and $V_{s,\ t}$ are both normalized by V_0 in the present analysis, thus $V_{0,\ n} = V_{0,\ t} = V_0$. In addition, the estimated uncertainty of the two dimensionless velocity components is 0.1.

Fig. 15 presents the variance of two splashing velocity components γ_n and γ_t with the roughness *St* increases. Note that since the velocities of secondary droplets keep changing due to gravity and air drag, only results at the time $\tau = 4.3$ are analysed and presented. From Fig. 15, it is seen that the dimensionless splashing velocity in the normal and tangential direction shows a different trend as *St* increases in the range $0.001 < St < 0.01$. Specifically, when $0.001 < St < 0.01$, the normal velocity of secondary droplet rises dramatically. This indicates that the dynamic lamella-substrate contact line is sensitive to roughness variation in this dimensionless roughness scale. The deeper 'valleys' of the surface roughness cause much more motion obstruction in the tangential direction, thus secondary droplets splash mainly toward the normal direction due to the reaction force during the impact. Also, the splashing velocity depends on the transfer of kinetic and surface energy of the incident droplet, and energy dissipation may have a significant change in this dimensionless roughness scale and influence the splashing.

For $0.01 < St < 0.1$, both the normal and tangential velocity of secondary droplets show an increasing trend with roughness rises, and the increasing degree of the tangential velocity is slightly smaller than that of the normal velocity. It is hypothesized that as *St* increases approximately from 0.01, the splashing regime may have changed from corona to prompt splashing, which could promote the kinetic energy transfer. In addition, "entrapped air pocket" or surrounding air may be another factor influencing the kinetic energy transfer behind the result (Latka et al., 2012; Tsai et al., 2010; Xu et al., 2007). This is a complex process and can be a topic for further analysis. The splashing velocity data on different surface roughness is fitted as following correlations within the present experimental conditions of $\theta_0 = 90°$ and $235 < K < 245$.

$$\begin{cases} \gamma_n = 0.448 + 0.0506lnSt \approx 0.3(1.49 + 0.169lnSt)\ (0.001 < St < 0.1) \\ \gamma_t = 0.25 - 0.226StlnSt \approx 1.075(0.233 - 0.21StlnSt)\ (0.01 < St < 0.1) \end{cases} \tag{13}$$

The splashing phenomenon is relatively minor on a smoother surface, as shown in Fig. 16, where the splashing holograms for case 6 ($St =$

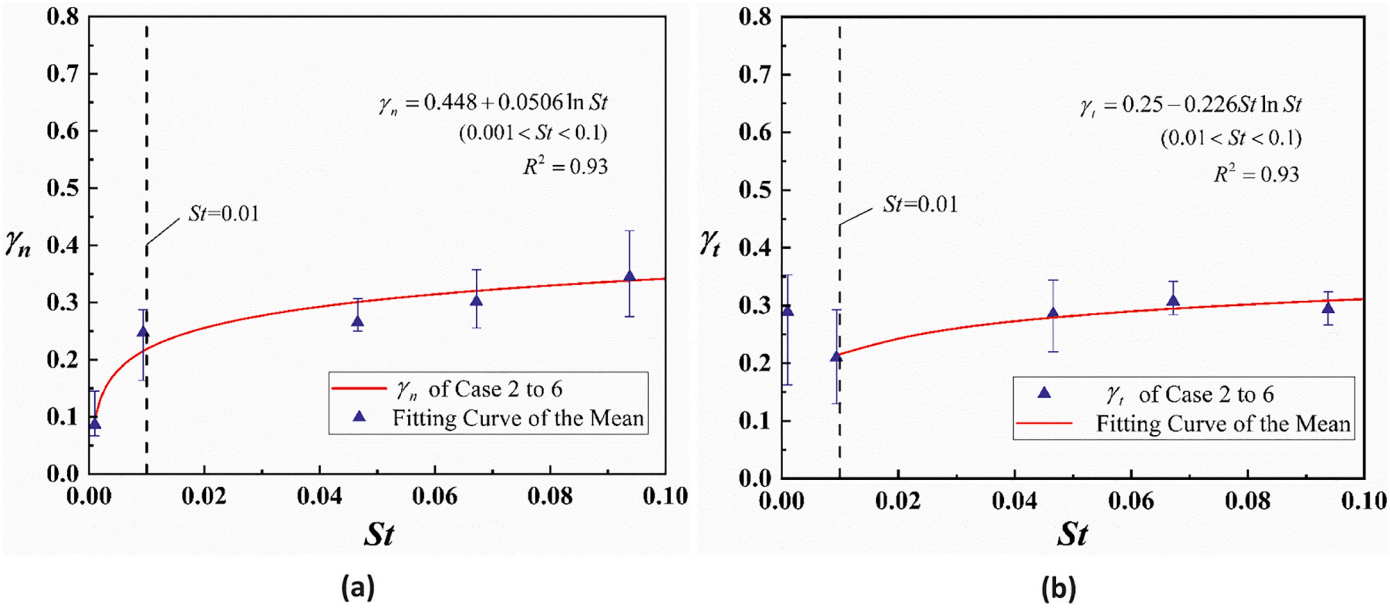

Fig. 15. (a) Relationship between normal splashing velocity γ_n and roughness St (b) Relationship between tangential splashing velocity γ_t and roughness St.

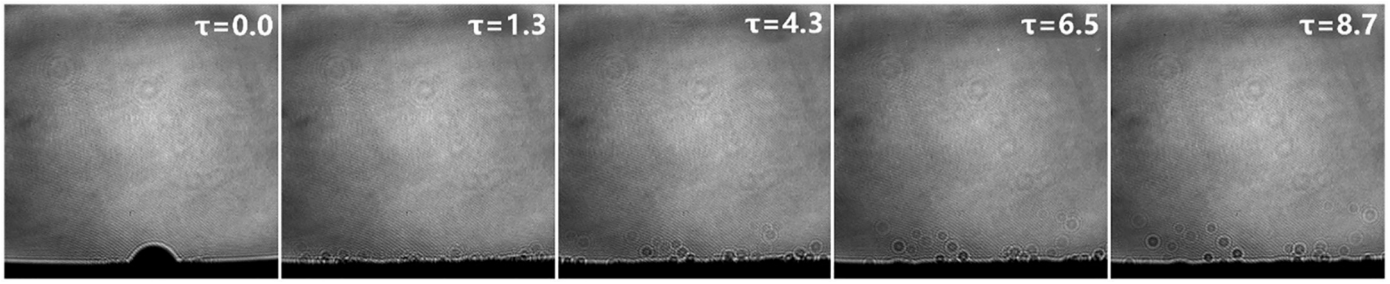

Fig. 16. Experimental hologram images of Case 6 (St = 0.001).

0.001) are presented. When surface roughness is reduced further to smooth sufficiently, the particle size becomes quite smaller than the water droplet size; thus, the tangential obstruction on secondary droplet disappears completely. In this case, the surface tension of the water droplet is large enough to keep the droplet sticking to the surface and no secondary droplets are produced, as shown in Fig. 9.

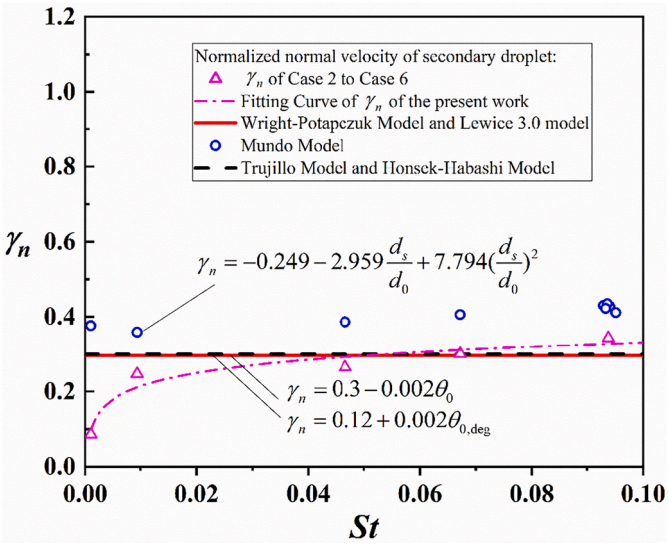

Fig. 17. Normal splashing velocity γ_n at different surface roughness.

We compare the correlation of normal velocity γ_n with the existing models in open literatures (Honsek, 2005; Mundo et al., 1997; Trujillo et al., 2000; Wright, 2005), as shown in Fig. 17. It is noted that there is no roughness effect in all the existing models. It can be seen that the results of γ_n for the existing models remain almost unchanged as St increases, while the present experimental data show a dramatic and gradual increase when $St < 0.01$ and $St > 0.01$, respectively. The present study indicates that surface roughness has effect on the characteristics of droplet splashing indeed and more accurate model should be developed by considering surface roughness.

Splashing angle is mainly influenced by the initial ejection angle of secondary droplets at the lamella-substrate contact line, which is also a macro-representation of the ratio between the normal and tangential velocity components of secondary droplets, and can be determined by $\theta_s = \tan^{-1}(V_{s,n}/V_{s,t})$. Fig. 18 shows the variation of the dimensionless splashing angles ϕ with St. The trend is quite similar to that of the normal splashing velocities with St. According to the findings of Quetzeri-Santiago et al. (2019a), the maximum dynamic contact angle generally increases with roughness. On the rougher surface, the secondary droplets are expected to splash with larger splashing angle ϕ. Moreover, when St decreases and is less than 0.01, the splashing angle drops sharply, which is another evidence that splashing is more sensitive in this dimensionless roughness scale.

3.2.3. Mass loss rates of secondary droplets

The mass loss rate directly reflects the severity of splashing and the

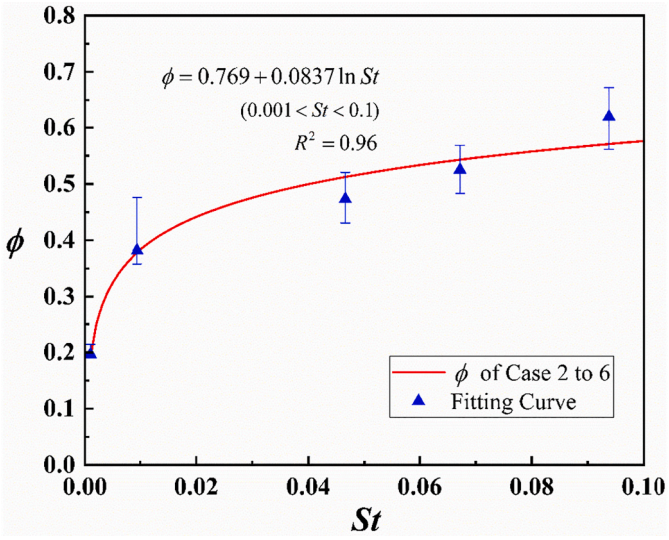

Fig. 18. Splashing angle ϕ corresponding to different surface roughness *St*.

mass of the residual water on the impact surface; the latter refers to the local water collection coefficient, an important factor that affects ice accretion on a body surface. In Fig. 19, the holograms of case 2d, 5 and 6 at $\tau = 1.3$ are shown to present the splashing droplet numbers N on different roughness surfaces. It is seen clearly that the number of splashing secondary droplets rises with *St*. The number of secondary droplets is validated against the model of Range and Feuillebois (1998) and Mehdizadeh et al. (2004) as shown in Fig. 20. Both models have the similar condition to present study. The number of secondary droplets is believed to be related closely to the estimation of mass loss. It is seen that for millimetre droplet, the number of perturbations decreases with roughness *Ra* when $Ra < 10\mu m$ but shows an opposite trend when $Ra > 1\mu m$. This indicates that, for $1\mu m < Ra < 10\mu m$, there may be a transition area from corona splashing to prompt splashing.

In most of the existing icing simulation codes, such as LEWICE and FENSAP, the mass loss rate f is only predicted as a function of impact parameter K under the same liquid water contents (LWC) and incident angle, while surface roughness is not accounted for. It is found that, however, there is no direct correlation between f and K when the roughness effect is considered according to the current experimental study, as shown in Fig. 18, where the mass loss rate was calculated at the earliest stable time $\tau = 4.3$. For example, at $K = 240.5 \pm 2.0$, mass loss rate could be as big as nearly 0.15 due to the effect of surface roughness for point A and B. Moreover, for point B and C in Fig. 21 having different values of K, they have a similar mass loss rate because of the similar surface roughness. Therefore, it can be concluded that, under the current experimental conditions, surface roughness has significant effect on mass loss rate of secondary droplets.

Fig. 22 shows the measured mass loss rate f corresponding to different surface roughness *St*, compared to the results calculated by Mundo model (Wright, 2005), that is $m_s/m_0 = n_s\left(\overline{d_s}/d_0\right)^3$. Note that Mundo developed this model at impact angle $\theta_0 < 90°$, which is different from the present work. Mass loss is found generally decreasing with impact angle (Bodoc and Berthoumieu, 2019). The comparison here is conservative, and as shown in Fig.22, the average uncertainty relative to the mass loss rate is approximately ± 0.0065. It is seen that f exhibits an approximately exponential growth with dimensionless roughness *St*. On a rougher surface, the coarser sand particles have greater obstruction on the spreading of the droplet film on the surface, thus the interaction between the coarser particles and the incident water droplet becomes stronger and dominant. It causes much more secondary droplets splashing in the normal direction, resulting in a greater loss of the incident droplet mass and thus a higher mass loss rate. A fitted correlation is obtained as below and the curve is plotted in Fig. 22:

$$f = 0.0037 - 6.016St^2 ln(St)\ 0.001 < St < 0.1 \text{ and } 235 < K < 245 \quad (14)$$

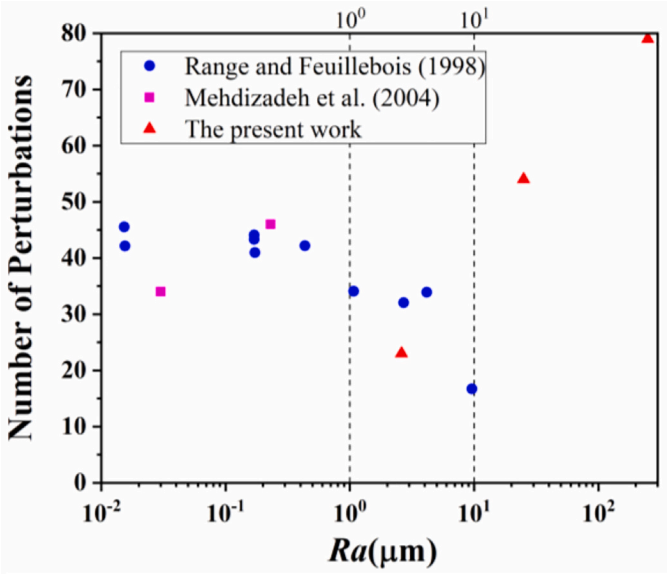

Fig. 20. Mass loss rate f on different surface roughness against impact parameter *K*.

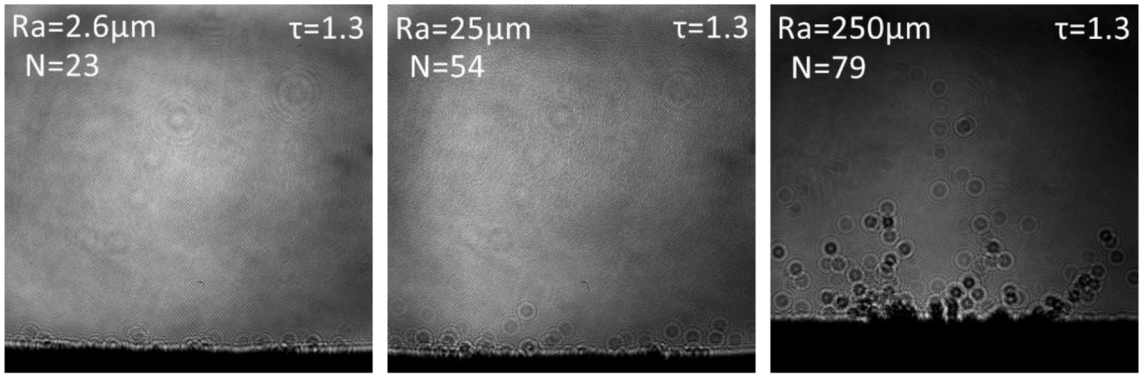

(a) Case 6 (St=0.001) **(b) Case 5 (St=0.0094)** **(c) Case 2d (St=0.0936)**

Fig. 19. Comparison of splashing droplet numbers on different roughness surface.

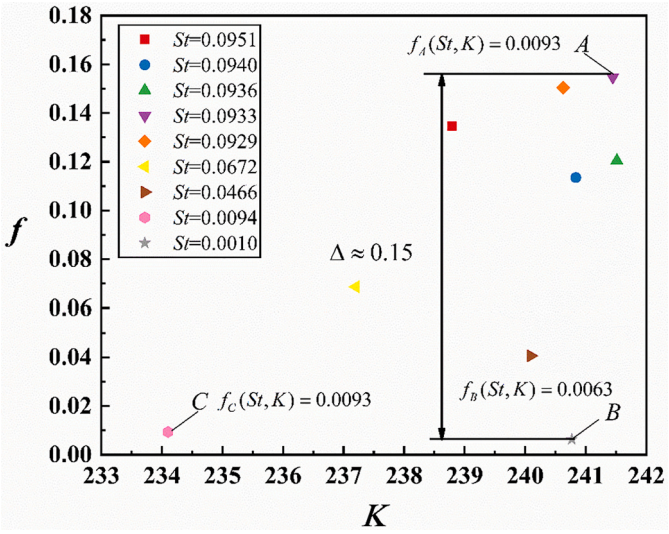

Fig. 21. Mass loss rate f on different surface roughness against impact parameter K.

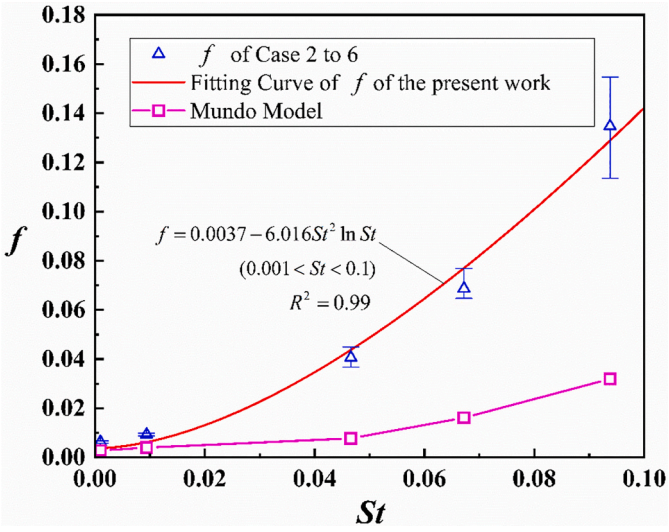

Fig. 22. Mass loss rate f corresponding to different surface roughness St.

f is less than 0.2 under the current experimental conditions.

3.2.4. Spatial distribution of secondary droplets

The spatial distribution very close to the surface at a certain instant is important for icing simulation because it would significantly affect the secondary droplets collection efficiency upon impact on the wings. In addition, the flow velocity increases rapidly within the boundary layer near the impact surface, so the interaction between secondary water droplets and airflow in each dimensionless-height layer is very different, particularly for the SLD icing prediction.

In the present study, a statistical analysis on splashing droplets mass distribution at selected splashing heights is carried out for four test cases, case 2a, 3, 5 and 6, at the selected time $\tau = 4.3$, as shown in Fig. 23. Here, the dimensionless height η is defined as $\eta = h/d_0$, where h is the y-direction coordinates of the secondary droplets. The diameters of all the secondary droplets in each dimensionless height are averaged and the mass ratio of secondary droplets in each layer to the total mass of all splashing droplets is evaluated.

In general, the average diameter and mass ratio of secondary droplets decrease as splashing height grows. For example, in the first height layer ($\eta = 1$) of case 2a as shown in Fig. 23 (a), the secondary droplets' mass ratio reaches the highest value of 0.72, which means up to $\tau = 4.3$ upon impact, more than 70% (mass) of the secondary droplets exists at the height equal to the incident droplet diameter d_0, with an average diameter of 250 μm. In the second layer ($\eta = 2$), only about 20% (mass) of the secondary droplets are distributed at the height equal to $2d_0$, but with the same average diameter of 250 μm. For the rest of the height layer units, both the splashing droplets diameter and the mass ratio drop dramatically. The similar distributions are found in case 3, 5 and 6 as well, as shown in Fig. 23 (b)-(d). This finding is attributed to a fact that greater gravity forces would exert on the bigger splashing droplet, resulting in a lower splashing height and larger mass ratio. In contrast, it would be easier for the smaller and lighter secondary droplets to overcome the gravity force and splash higher. It is noted that the results may be different when applied in aircraft icing because of the presence of a high velocity airflow. The smaller droplets with less inertia will be carried away by the high speed flow more easily than the larger droplets, and thus cause the different distribution.

From Fig. 23, it is found that with reduced roughness (from case 2a to 6), the mass ratio in the first height layer is increasing from approximately 0.72 to 0.98, which indicates that on the smoother surface, much more secondary droplets splash at a lower splashing height. In case 2a and 3, 95% (mass) of the secondary droplets splash in the first and second height layer units, whereas in case 5 and 6, 97% (mass) of the secondary droplets are distributed in the first layer only. In case 6 where the surface is least rough, the maximum splashing height is only twice of the incident droplet diameter, while in other cases the maximum splashing height is five times of the incident diameter. In short, on the smoother surface, the diameter, normal velocity component, angle and height of the splashed droplets decrease, resulting in a decrease in the average diameter and an increase in the mass ratio in the first height layer unit.

4. Conclusions

An experimental study on the effects of surface roughness on large droplet splashing behaviours is performed by using DIH aiming to collect the 3D information of the secondary droplets. The following conclusions are obtained:

(1) Results show DIH is suitable for diagnosing micro-sized transparent droplets in splashing. The three-dimensional splashing fields of the secondary droplets are reconstructed by a wavelet-based algorithm. Compared to high-speed camera, DIH can capture more 3D information and features of secondary droplets. It has a higher accuracy in recording the secondary droplets splashing characteristics.

(2) The splashing characteristics of the secondary droplets' diameters at different dimensionless roughness ranging between [0.001, 0.1] and the empirical correlations are obtained and developed. To be specific, splashing characteristics are sensitive to the roughness with $St \approx 0.01$, and St around 0.01 is proposed to be a critical roughness for further splashing analysis.

(3) The mass ratio and average diameters of secondary droplets in each dimensionless splashing height at certain time ($\tau = 4.3$) are analysed statistically and presented in histogram. In the present experimental conditions with $0.001 < St < 0.1$, more than 90% (mass) of the secondary droplets stay within the first two dimensionless heights at time $\tau = 4.3$. This finding could support the motion simulation of secondary droplets in the boundary layer.

(4) It is noted that the similarity of droplet impact and splashing process have not been known very well yet. The effect of roughness on secondary droplets found in our experiments has its limitation if applied to smaller droplets (less than 1 mm diameter) and higher impact velocity or Weber number. It is recommended

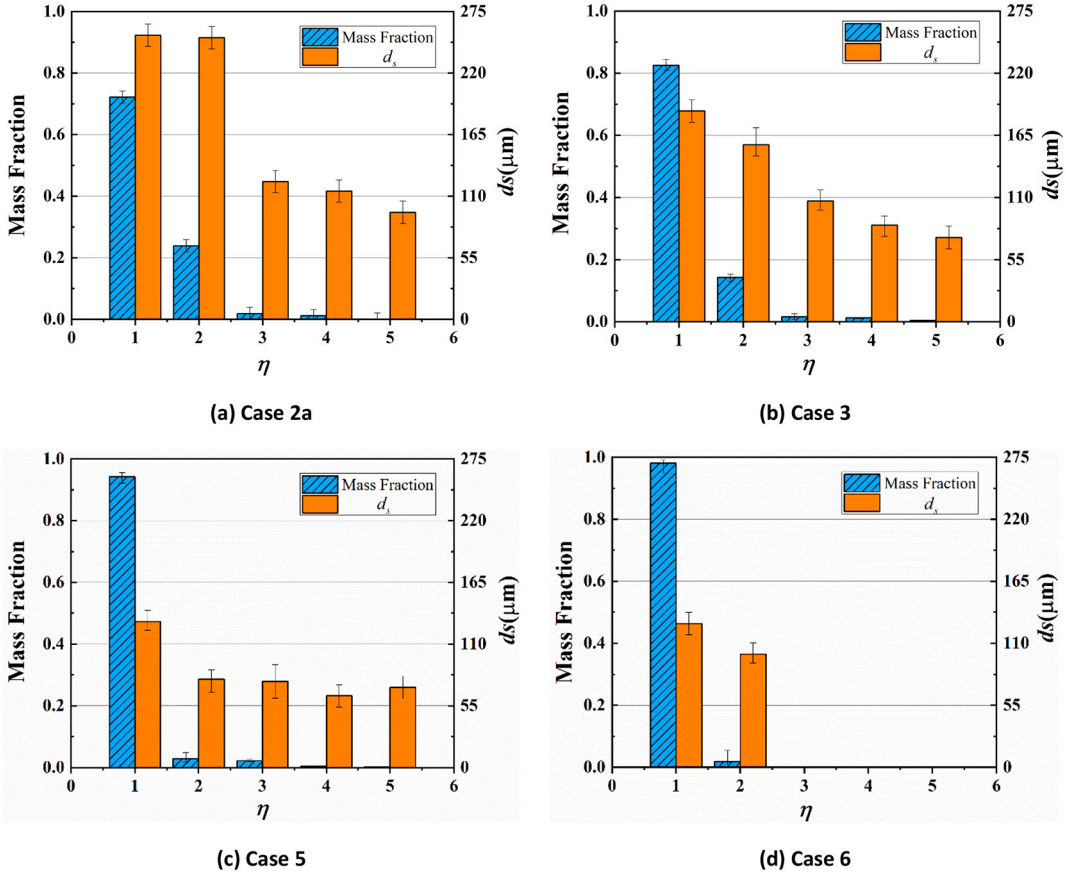

Fig. 23. Splashing height distributions of secondary droplets ($\tau = 4.3$).

to use the present results at similar condition, especially the same *We* number and Oh number. Also, experimental validation should be performed if the experimental conditions is out of the present work. It is noted that different definition on surface roughness may cause different results.

Our study is supposed to have contribution to further development of SLD icing simulation and may potentially be applied in the industrial applications, such as inkjet printing, spray, erosion and formation of ice layers. Further studies are necessary to investigate the effect of surface roughness on splashing characteristics with smaller droplet and higher impact speed. Also, low temperature effect is recommended to be studied experimentally.

Declaration of Competing Interest

The authors declare that they have no known competing financial interests or personal relationships that could have appeared to influence the work reported in this paper.

Acknowledgement

This work is supported by the National Natural Science Foundation of China (Grant No.11372335) and the Special Scientific Research Project of China (MJ-2016-F-07). Thanks to Dr. Longchao Yao and Mr. Zhiliang Xue from State Key Laboratory of Clean Energy Utilization of Zhejiang University for their technical support of the DIH measurement. Also, thanks to Ifrah for proof-reading.

References

Belaud, V., Valette, S., Stremsdoerfer, G., Bigerelle, M., Benayoun, S., 2015. Wettability versus roughness: multi-scales approach. Tribol. Int. 82, 343–349. https://doi.org/10.1016/j.triboint.2014.07.002.

Bhushan, B., 2000. Surface roughness analysis and measurement techniques. In: Modern Tribology Handbook, Two Volume Set. CRC press, pp. 79–150.

Bodoc, V., Berthoumieu, P., 2019. Experimental Investigation of High Speed SLD Impact. https://doi.org/10.4271/2019-01-2006.

Castrejón-Pita, J.R., Muñoz-Sánchez, B.N., Hutchings, I.M., Castrejón-Pita, A.A., 2016. Droplet impact onto moving liquids. J. Fluid Mech. 809, 716–725. https://doi.org/10.1017/jfm.2016.672.

Cimpeanu, R., Papageorgiou, D.T., 2018. Three-dimensional high speed drop impact onto solid surfaces at arbitrary angles. Int. J. Multiph. Flow 107, 192–207. https://doi.org/10.1016/j.ijmultiphaseflow.2018.06.011.

Cossali, G.E., Coghe, A., Marengo, M., 1997. The impact of a single drop on a wetted solid surface. Exp. Fluids 22, 463–472. https://doi.org/10.1007/s003480050073.

Crittenden, John C., Trussell, R. Rhodes, Hand, David W., Howe, Kerry J., Tchobanoglous, George, 2012. MWH's Water Treatment: Principles and Design, Third ed.

De Goede, T., De Bruin, K., Shahidzadeh, N., Bonn, D., 2020. Droplet Splashing on Rough Surfaces, pp. 1–8.

EASA, 2015. Certification Specifications and Acceptable Means of Compliance for Large Aeroplanes CS-25. Cs-25.

Guildenbecher, D.R., Engvall, L., Gao, J., Grasser, T.W., Reu, P.L., Chen, J., 2014. Digital in-line holography to quantify secondary droplets from the impact of a single drop on a thin film. Exp. Fluids 55. https://doi.org/10.1007/s00348-014-1670-3.

Honsek, R., 2005. Development of a Three-dimensional Eulerian Model of Droplet-wall Interaction Mechanisms. McGill University.

JCGM, J, et al., 2008. Evaluation of Measurement Data—Guide to the Expression of Uncertainty in Measurement, 50. Int. Organ. Stand, Geneva, p. 134.

Josserand, C., Thoroddsen, S.T., 2016. Drop impact on a solid surface. Annu. Rev. Fluid Mech. 48, 365–391. https://doi.org/10.1146/annurev-fluid-122414-034401.

Latka, A., Strandburg-Peshkin, A., Driscoll, M.M., Stevens, C.S., Nagel, S.R., 2012. Creation of prompt and thin-sheet splashing by varying surface roughness or increasing air pressure. Phys. Rev. Lett. 109, 054501 https://doi.org/10.1103/PhysRevLett.109.054501.

Levin, Z., 1970. Splashing of Water Drops: A Study of the Hydrodynamics and Charge Separation. University of Washington, Seattle, USA.

Li, J., Zhang, H., Liu, Q., 2019. Characteristics of secondary droplets produced by a single drop impacting on a static liquid film. Int. J. Multiph. Flow 119, 42–55. https://doi.org/10.1016/j.ijmultiphaseflow.2019.06.015.
Luxford, G., 2005. Experimental and Modelling Investigation of the Deformation, Drag and Break-up of Drizzle Droplets Subjected to Strong Aerodynamic Forces in Relation to SLD Aircraft Icing. Cranfield University.
Mehdizadeh, N.Z., Chandra, S., Mostaghimi, J., 2004. Formation of fingers around the edges of a drop hitting a metal plate with high velocity. J. Fluid Mech. 510, 353–373. https://doi.org/10.1017/S0022112004009310.
Moreira, A.L.N., Moita, A.S., Panão, M.R., 2010. Advances and challenges in explaining fuel spray impingement: how much of single droplet impact research is useful? Prog. Energy Combust. Sci. 36, 554–580. https://doi.org/10.1016/j.pecs.2010.01.002.
Mundo, C., Sommerfeld, M., Tropea, C., 1995. Droplet-wall collisions: Experimental studies of the deformation and breakup process. Int. J. Multiph. Flow 21, 151–173. https://doi.org/10.1016/0301-9322(94)00069-V.
Mundo, C., Tropea, C., Sommerfeld, M., 1997. Numerical and experimental investigation of spray characteristics in the vicinity of a rigid wall. Exp. Thermal Fluid Sci. 15, 228–237. https://doi.org/10.1016/S0894-1777(97)00015-0.
Pan, K.-L., Tseng, K.-C., Wang, C.-H., 2010. Breakup of a droplet at high velocity impacting a solid surface. Exp. Fluids 48, 143–156. https://doi.org/10.1007/s00348-009-0697-3.
Papadakis, M., Wong, S.-H., 2006. Parametric investigation of a bleed air ice protection system. In: 44th AIAA Aerospace Sciences Meeting and Exhibit. American Institute of Aeronautics and Astronautics, Reston, Virigina. https://doi.org/10.2514/6.2006-1013.
Papadakis, M., Rachman, A., Wong, S., Yeong, H., Bidwell, C.S., 2007a. Water Droplet Impingement on Simulated Glaze, Mixed, and Rime Ice Accretions (Nasa/Tm-2007-213961).
Papadakis, M., Wong, S.-C., Rachman, A., Hung, K.E., Vu, G.T., Bidwell, C.S., 2007b. Large and Small Droplet Impingement Data on Airfoils and Two Simulated Ice Shapes. NASA/TM—2007-213959.
Papadakis, M., Zumwalt, G., Kim, J., Elangovan, R., Freund Jr., G., 2013. An Experimental Method for Measuring Droplet Impingement Efficiency on Two- and Three-dimensional Bodies. https://doi.org/10.2514/6.1986-406.
Pegg, M., Purvis, R., Korobkin, A., 2018. Droplet impact onto an elastic plate: a new mechanism for splashing. J. Fluid Mech. 839, 561–593. https://doi.org/10.1017/jfm.2018.60.
Popinet, S., 2003. Gerris: a tree-based adaptive solver for the incompressible Euler equations in complex geometries. J. Comput. Phys. 190, 572–600. https://doi.org/10.1016/S0021-9991(03)00298-5.
Popinet, S., 2009. An accurate adaptive solver for surface-tension-driven interfacial flows. J. Comput. Phys. 228, 5838–5866. https://doi.org/10.1016/j.jcp.2009.04.042.
Quetzeri-Santiago, M.A., Castrejón-Pita, A.A., Castrejón-Pita, J.R., 2019a. The effect of surface roughness on the contact line and splashing dynamics of impacting droplets. Sci. Rep. 9, 15030. https://doi.org/10.1038/s41598-019-51490-5.
Quetzeri-Santiago, M.A., Yokoi, K., Castrejón-Pita, A.A., Castrejón-Pita, J.R., 2019b. Role of the dynamic contact angle on splashing. Phys. Rev. Lett. 122, 228001. https://doi.org/10.1103/PhysRevLett.122.228001.
Range, K., Feuillebois, F., 1998. Influence of surface roughness on liquid drop impact. J. Colloid Interface Sci. 203, 16–30. https://doi.org/10.1006/jcis.1998.5518.
Roisman, I.V., Lembach, A., Tropea, C., 2015. Drop splashing induced by target roughness and porosity: the size plays no role. Adv. Colloid Interf. Sci. 222, 615–621. https://doi.org/10.1016/j.cis.2015.02.004.
Skrondal, B., Everitt, A., 2010. The Cambridge Dictionary of Statistics, 4th ed. Cambridge University Press, Cambridge. https://doi.org/10.1002/(sici)1097-4598(199906)22:6<783::aid-mus21>3.3.co;2-f.
Stow, C.D., Hadfield, M.G., 1981. An experimental investigation of fluid flow resulting from the impact of a water drop with an unyielding dry surface. Proc. R. Soc. A Math. Phys. Eng. Sci. 373, 419–441. https://doi.org/10.1098/rspa.1981.0002.
Stow, C., Stainer, R., 1977. The physical products of a splashing water drop. Meteorol. Soc. Jpn. J. 55, 518–532.
Tang, C., Qin, M., Weng, X., Zhang, X., Zhang, P., Li, J., Huang, Z., 2017. Dynamics of droplet impact on solid surface with different roughness. Int. J. Multiph. Flow 96, 56–69. https://doi.org/10.1016/j.ijmultiphaseflow.2017.07.002.
Thoroddsen, S.T., Etoh, T.G., Takehara, K., 2008. High-speed imaging of drops and bubbles. Annu. Rev. Fluid Mech. 40, 257–285. https://doi.org/10.1146/annurev.fluid.40.111406.102215.
Trujillo, M.F., Mathews, W.S., Lee, C.F., Peters, J.E., 2000. Modelling and experiment of impingement and atomization of a liquid spray on a wall. Int. J. Engine Res. 1, 87–105.
Tsai, P., Van Der Veen, R.C.A., Van De Raa, M., Lohse, D., 2010. How micropatterns and air pressure affect splashing on surfaces. Langmuir 26, 16090–16095. https://doi.org/10.1021/la102330e.
Van Zante, J.F., 2007. A Database of Supercooled Large Droplet Ice Accretions. https://doi.org/10.4271/2007-01-3348.
Weiss, C., 2005. The liquid deposition fraction of sprays impinging vertical walls and flowing films. Int. J. Multiph. Flow 31, 115–140. https://doi.org/10.1016/j.ijmultiphaseflow.2004.08.004.
Wierzba, A., 1990. Deformation and breakup of liquid drops in a gas stream at nearly critical Weber numbers. Exp. Fluids 9, 59–64. https://doi.org/10.1007/BF00575336.
Worthington, A., 1877. On the forms assumed by drops of liquids falling vertically on a horizontal plate. Proc. R. Soc. Lond. 25, 261–272. https://doi.org/10.1098/rspl.1876.0048.
Wright, W., 2005. Validation results for LEWICE 3.0. In: 43rd AIAA Aerospace Sciences Meeting and Exhibit. American Institute of Aeronautics and Astronautics, Reno, Nevada, pp. 1–26. https://doi.org/10.2514/6.2005-1243.
Wright, W.B., 2008. User's Manual for LEWICE Version 3.2. Nasa/Cr-2008-214255 (doi: 20080048307).
Wright, W., Potapczuk, M., 2004. Semi-empirical modelling of SLD physics, in: 42nd AIAA Aerospace Sciences Meeting and Exhibit. American Institute of Aeronautics and Astronautics, Reno, Nevada. doi:https://doi.org/10.2514/6.2004-412.
Wu, Z., 1992. Mode'lisation et calcul implicite multidomaine d'e'coule- ments diphasiques gaz-gouttelettes. Universite' Pierre et Marie Curie.
Wu, Y., Wu, X., Yang, J., Wang, Z., Gao, X., Zhou, B., Chen, L., Qiu, K., Gréhan, G., Cen, K., 2014. Wavelet-based depth-of-field extension, accurate autofocusing, and particle pairing for digital inline particle holography. Appl. Opt. 53, 556. https://doi.org/10.1364/AO.53.000556.
Wu, Y., Yao, L., Wu, X., Chen, J., Gréhan, G., Cen, K., 2017. 3D imaging of individual burning char and volatile plume in a pulverized coal flame with digital inline holography. Fuel 206, 429–436. https://doi.org/10.1016/j.fuel.2017.06.031.
Xu, L., Barcos, L., Nagel, S.R., 2007. Splashing of liquids: Interplay of surface roughness with surrounding gas. Phys. Rev. E 76, 066311. https://doi.org/10.1103/PhysRevE.76.066311.
Yao, L., Wu, X., Wu, Y., Yang, J., Gao, X., Chen, L., Gréhan, G., Cen, K., 2015. Characterization of atomization and breakup of acoustically levitated drops with digital holography. Appl. Opt. 54, A23. https://doi.org/10.1364/ao.54.000a23.
Yao, L., Chen, J., Sojka, P.E., Wu, X., Cen, K., 2018. Three-dimensional dynamic measurement of irregular stringy objects via digital holography. Opt. Lett. 43, 1283. https://doi.org/10.1364/OL.43.001283.
Yarin, A.L., 2006. Drop Impact Dynamics: Splashing, Spreading, Receding, Bouncing…. Annu. Rev. Fluid Mech, 38, pp. 159–192. https://doi.org/10.1146/annurev.fluid.38.050304.092144.
Yarin, A.L., Weiss, D.A., 1995. Impact of drops on solid surfaces: self-similar capillary waves, and splashing as a new type of kinematic discontinuity. J. Fluid Mech. 283, 141–173. https://doi.org/10.1017/S0022112095002266.